Tribology International 210 (2025) 110792

Contents lists available at ScienceDirect

Tribology International

journal homepage: www.elsevier.com/locate/triboint

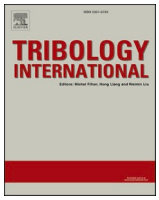

Effect of ultrasonic nanocrystal surface modification on microstructural evolution and tribological properties of pure tungsten

M. Zohrevand [a], J. Likonen [b], J.W. Coenen [c,d], A. Amanov [a,*]

[a] Faculty of Engineering and Natural Sciences, Tampere University, PO Box 589, Tampere FIN-33014, Finland
[b] VTT Technical Research Centre of Finland, VTT, PO Box 1000, FIN-02044, Finland
[c] Forschungszentrum Jülich GmbH, Institute for Fusion Energy and Nuclear Waste Management, Jülich 52425, Germany
[d] Department of Nuclear Engineering & Engineering Physics – UW Madison, Madison, USA

ARTICLE INFO

Keywords:
Tungsten
Grain refinement
Tribology
Surface modification

ABSTRACT

The effects of the ultrasonic nanocrystal surface modification (UNSM) treatment on the microstructure, mechanical properties, and tribological behavior of the pure tungsten (W) were investigated. The tribological properties of W were evaluated under dry sliding conditions and the coefficient of friction (COF) was reduced from 0.62 for the untreated sample to 0.5 and 0.42 after the UNSM treatment with reference and optimized conditions, respectively. A significant improvement of 38 % in the wear resistance was achieved for the UNSM treatment with optimized conditions. It was found that the wear mechanisms shift from severe abrasive and adhesive wear to primarily mild abrasive wear with a substantial reduction in wear severity.

1. Introduction

Given its substantially lower energy consumption, ultrasound is classified as a green technology [1]. It has been extensively employed in materials processing and manufacturing processes for decades. The industrial applications encompass a wide range of sectors, including, but not limited to, metals casting [2,3], metal forming [4,5], welding [6,7], and machining [8,9]. Ultrasound has also been utilized as a post-processing technique for modifying the microstructure and improving the properties of materials [10–12]. Acoustic softening [13], reduction in friction coefficient [14], residual stress removal [15], and homogenization of molten metals [16] have been mentioned as the main physical effects of ultrasonic vibration, enabling its wide range of applications in the manufacturing chain.

Extensively studied in numerous research endeavors over the past decades, the ultrasonic nanocrystal surface modification (UNSM) technique stands as a highly advanced application of ultrasounds in materials processing [17]. This process involves inducing surface severe plastic deformation (S^2PD) on the material's surface by applying a static load with repetitive impacts from a hard material (typically tungsten carbide - WC) vibrating at an ultrasound frequency of 20 kHz [18]. Utilizing this process, mechanical properties can be enhanced by tailoring the surface microstructure into the ultrafine-grained (UFG), a formation of a gradient structure, and the high density of defects like dislocations, twins, and stacking faults [19]. Structure modification in this process is associated with a remarkable increase in surface hardness [20], beneficial compressive residual stress [21], and a reduction in the surface roughness and friction coefficient [22].

The major advantage of the UNSM treatment is the significant improvement in the fatigue lifetime of materials, which may be mainly attributed to the compressive residual stress and the formation of the UFG structure within the surface layer [23]. Significant surface hardening at a wide range of materials introduced the UNSM treatment as an effective method for improving tribological properties [24]. Inducing the higher corrosion resistance is another advantage of the UNSM treatment, which has been reported in the literature [25]. In 17–4PH stainless steel, the (110) and (211) textures, in addition to reduced surface roughness, have been mentioned as reasons for improved corrosion resistance [26]. The UNSM treatment has also been utilized to reduce surface porosities following additive manufacturing [27]. As one of the most recent applications, UNSM has been shown as an effective technique for enhancing the resistance of materials against hydrogen embrittlement [28].

Tungsten (W), a refractory metal with one of the highest melting points and density among all elements, has extensive applications across various industries. The applications include the production of high-

* Corresponding author.
E-mail address: auezhan.amanov@tuni.fi (A. Amanov).

https://doi.org/10.1016/j.triboint.2025.110792
Received 18 December 2024; Received in revised form 12 February 2025; Accepted 6 May 2025
Available online 7 May 2025

performance electrodes for lighting industries [29], thin films in semiconductors [30], catalysts for environmental applications [31], and plasma-facing components in fusion reactors [32,33]. The attention towards microstructure tailoring to create a nanostructured W has significantly increased in recent decades due to its superior performance and extended lifespan. It has been proven that nanostructured W has a higher radiation resistance since grain boundaries act as effective sites for trapping defects and releasing He atoms [34]. Various methods like powder metallurgy [35], equal channel angular extrusion (ECAP) [36], and high-pressure torsion (HTP) [37] have been employed for the manufacturing of bulk UFG W. Nevertheless, due to the limited size of components by such processes, surface modification techniques have also been evaluated in this regard. Efe et al. [38] examined the grain refinement in pure W through surface deformation by machining. Gou et al. [39,40] employed surface mechanical attrition treatment (SMAT) for creating the nanocrystalline grain structure in W. Their results showed that the SMAT-treated W had greater hardness, bending strength, compressive residual stress, and toughness compared to the coarse-grained W. In a very recent research, Wang et al. [41], combined mechanical grinding and thermal annealing to achieve a UFG structure on the surface of pure W.

W and its alloys are also a material option for tribological applications due to their pronounced wear resistance, especially at elevated temperatures [42]. It has been shown that the tribological properties of W are extremely related to the initial microstructure and environment temperature [43,44]. Jiang et al. [45] investigated the tribological behavior of W in the temperature range of 25–1000 °C. They reported a decrease in the friction coefficient as a function of time and temperature and observed a maximum wear rate at 250 °C. Ding et al. [46] explored the correlation between microstructure, temperature, and wear behavior of W. They showed that at elevated temperatures sub-grains evolved from low-angle grain boundaries (LAGBs) to high-angle grain boundaries (HAGBs), where the wear rate was reduced due to the improved deformability and generation of oxide layers.

Despite the previously conducted research on methods like laser shock peening (LSP) of pure W [47] and ultrasonic surface treatment of W heavy alloy [48], there is still a lack of information on the surface modification of W alloys. In the present work, for the first time, we investigated the effect of UNSM treatment on the microstructure and tribological properties of commercial pure W. Providing a detailed microstructural characterization, the grain refinement mechanisms, texture evolution, tribological properties and the optimum UNSM treatment parameters have been reported and discussed. The results obtained from this work aim to develop a new technique for surface modification of pure W and even other refractory hard metals to create a nanostructured surface layer, which can be utilized in various related applications.

2. Materials and methods

2.1. Sample preparation

The pure W samples with dimensions of 10 × 10 × 4.8 mm^3 were provided by the manufacturer Plansee Group Functions Austria GmbH [49]. The sample were produced by powder metallurgy (PM) and normalized by forging. The forged samples were exposed to a stress relieving treatment by thermal annealing. The production process results in a grain structure that is highly elongated, forming needle-like grains aligned parallel to the forging direction, with diameters of 5–10 μm and lengths of approximately 25 μm [50]. The purity of the sample was > 99.97 of W in wt% and the remaining portion consists of the primary elements listed in Table 1.

2.2. UNSM treatment

The UNSM treatment was carried out on the top surface of the W samples at different static loads, vibration amplitudes, and scanning numbers, as given in Table 2 for each sample. A 2.38 mm in diameter semi-spherical WC was utilized as a tip. The UNSM treatment setup and scanning strategy for the experiments are schematically displayed in Fig. 1. A constant scanning speed of 1000 mm/min was used for all the samples. The second UNSM scan for the samples #S3, #S4 and #S7 was conducted in the perpendicular direction compared to the initial scan, as shown in Fig. 1 (hereafter these samples will be referred to as cross-scanned samples). Continuous air blowing was provided during the UNSM treatment to keep the surface clean and to prevent local heating at the contact interface. The UNSM treatment has already been applied to tantalum (Ta), which is a refractory metal, with a melting point above 2000 ^{0}C [51].

2.3. Roughness, hardness, and residual stress

The surface roughness and wear track dimensions of the samples were measured using an optical 3D surface profilometer (Alicona InfiniteFocus G5, Bruker, Austria). The hardness of the samples was measured using a microhardness tester (Duramin-A300, Struers, Denmark) at a load of 980 mN and a dwell time of 15 sec. The residual stress of the samples was measured using an XStress 3000 G2 portable device (Stresstech Inc., USA). Measurement parameters for W with CrKα radiation: diffraction angle 125° referring to [211] lattice plane, Poisson`s ratio of 0.27, Young`s modulus of 400 GPa.

2.4. FE-SEM and EBSD characterizations

The electron microscopy investigation was carried out using a field emission scanning electron microscope (FE-SEM: Zeiss UltraPlus, Germany) equipped with Oxford Instruments Symmetry electron-backscattered diffraction (EBSD: Oxford Instruments, UK) and energy dispersive spectroscopy (EDS: X-MaxN 80, Oxford Instruments, UK) detectors. The results were further post-processed by Oxford AZtec-Crystal software (version 3.1). For EBSD sample preparation, the cross-section of the samples (perpendicular to the scanning plane) was polished through the standard method followed by the final polishing via 0.25 μm colloidal silica suspension. An acceleration voltage of 20 kV, working distances of 15 mm (for EBSD) and 8.5 mm (for EDS), step sizes of 50 nm (for higher magnifications scans) and 200 nm (for lower magnification scans) were chosen as parameters for EDS-EBSD analysis. The inverse pole figures (IPF) maps were extracted along the X-direction parallel to the scanning direction. The densities of geometrically necessary dislocations (GND) were calculated for $a/2 < 110 >$ Burger's

Table 2
Selected UNSM treatment parameters used in the experiments.

Sample ID	#S1	#S2	#S3	#S4	#S5	#S6	#S7
Static load (N)	50	65	50	65	50	50	50
Vibration amplitude (μm)	30	30	30	30	40	50	40
Number of scans (repetitions)	1	1	2	2	1	1	2

Table 1
Chemical composition of pure W sample [49].

Al	Fe	Si	Cd	Cr	K	Mo	N	Cu	Ni	C	O	Pb
1	8	1	1	3	1	12	1	1	2	6	2	1

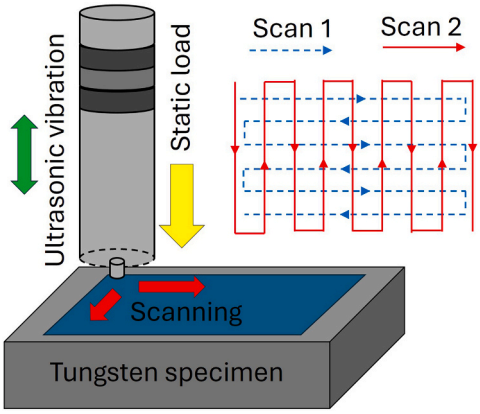

Fig. 1. Schematic view of the UNSM treatment setup and the scanning strategy used in this study.

vector and α= 3 as the constant value using a 3 × 3 Kernel size. The 10° was used as the HAGB threshold for calculating the grain size.

2.5. Tribological properties

The tribological properties of the samples were carried out using a universal tribometer (Nanovea T2000, USA) under dry conditions in accordance with ASTM G133–05 standard. The tribo testing conditions are listed in Table 3. During the testing, the coefficient of friction (COF) was recorded. The specific wear rate (SWR) of the samples was quantified according to the wear volume, applied normal load, and total sliding distance. The wear volume of the samples was calculated using the depth and width of the wear track. The tribo tests were repeated to ensure data repeatability and effectiveness of UNSM treatment on frictional behavior and wear resistance. In this study, an average value of the COF and SWR data was reported.

3. Results and discussion

3.1. Microstructural evolution

The initial microstructure of the as-received (untreated) sample is shown in Fig. 2. As can be seen in Fig. 2(a), the as-received sample shows a columnar structure including parallel pillars with the same crystallographic texture. Such a structure can be explained by the directional pressing and sintering procedures during the manufacturing of the samples through the conventional PM process. It is worth mentioning here that the columnar structure perpendicular to the surface was specifically designed to minimize the de-lamination. With higher magnification in Fig. 2(c), it is revealed that each pillar involves smaller grains with an average size of 4.54 μm (Table 4). As represented by the GND dislocation map in Fig. 2(d), the grain interior is almost free of dislocations, grain boundaries look smooth, and the triple point angles are close to the equilibrium value of 120°, indicating a fully annealed structure.

Table 3
Tribo testing conditions.

Applied normal load (N)	10
Reciprocating linear speed (mm/min)	500
Stroke (mm)	5
Duration (min)	10
Environment	Dry and room temperature
Counter ball material	Stainless steel 440
Counter ball diameter (mm)	6

3.1.1. Effect of static load

The cross-sectional EBSD images of samples #S1 and #S2 with two different magnifications are depicted in Fig. 3 showing the influence of the static load of the UNSM treatment on microstructure. Considering the higher magnification images in Fig. 3(b and e), the UNSM treatment resulted in S^2PD in the topmost surface of the samples, and accordingly, a large number of LAGBs have been formed. Based on the GND map in Fig. 3(c and f), it can be seen that the dislocation density has been significantly increased in the top-surface region of the treated samples. Unlike the #S1 sample, a sheared structure (highlighted by dashed lines in Fig. 3(d)) has been formed in the #S2 sample, as a result of using a higher static load. According to Fig. 3 and the statistical information given in Table 4, it was revealed that by a 30 % increase in the static force from 50 N to 65 N, the LAGB fraction and GND density were increased by 14 % and 7 %, respectively. Comparing #S1 and #S2 samples in Fig. 3, one can identify that increasing the static load of UNSM treatment mainly resulted in greater dislocation densities and LAGBs fraction and it did not change the microstructure morphology as well as grain refinement depth in pure W.

3.1.2. Effect of cross-UNSM scanning

The influence of the second UNSM scanning was explored and the obtained results for the samples #S3 and #S4 are presented in Fig. 4. Based on Table 2, similar UNSM treatment parameters of the samples #S1 and #S2 were used for the samples #S3 and #S4, but with repeating the scan in a perpendicular direction. As can be observed in Fig. 4(a and f), the UNSM cross-scanning led to a significant distortion, and a wavy structure was formed with estimated depths of 160 μm and 190 μm, respectively for the samples #S3 and #S4. According to Fig. 4(a-e), the UNSM cross-scanning of the sample #S3 resulted in de-lamination, which can be attributed to the brittle characteristics of W. A similar de-lamination has been reported by Gou et al. [39,40] during the SMAT treatment of W. According to Fig. 4(b and c), the laminates at the top surface region indicate a fibrous structure, and the elongated grains encompass a large density of dislocations due to the remarkable compressive deformation. On the other hand, the subsurface region (Fig. 4(d and e)) represents a remarkably different microstructure including equiaxed newly formed grains with low to medium-angle grain boundaries (MAGBs) within the elongated old grains with HAGBs. According to the EBSD data given in Table 4, the laminated area (#S3–1) has higher dislocation density, but a lower LAGB fraction, compared to the subsurface region (#S3–2). The de-lamination at the top surface of the #S3 sample can be attributed to the outstanding compressive deformation at the top surface region during the second UNSM scanning. It seems that by the significant increase in the dislocation density, the work hardening capacity of W, which is known as a relatively brittle metal, has been exhausted and consequently de-lamination failure happened. On the other hand, the formation of the sub-grains and the lower dislocation density in the subsurface region (Fig. 4(d and e)) exhibits a progressive dynamic recovery during the multiple UNSM scan. Such a process can be explained through the polygonization of initial dislocations formed during the first scan and the developed recovery throughout the second UNSM scan.

Unlike the #S3 sample, the de-laminated region is not visible in the #S4 sample, and the microstructure of the top surface is like those observed in the subsurface area in the #S3 sample. In this condition, the top surface area of the #S4 sample exhibits a large fraction of LAGBs and MAGBs with an increased density of dislocations (Fig. 4(g and h)). According to the reported data in Table 4, the dislocation density and the fraction of LAGBs and MAGBs in the #S4 sample are very close to the subsurface region of the #S3 sample (#S3–2). Based on these observations, it can be interpreted that using higher static loads in the multiple UNSM scanning does not improve the microstructure and dislocation density and only results in more severe delamination in a way that the laminated layers were removed during the UNSM treatment.

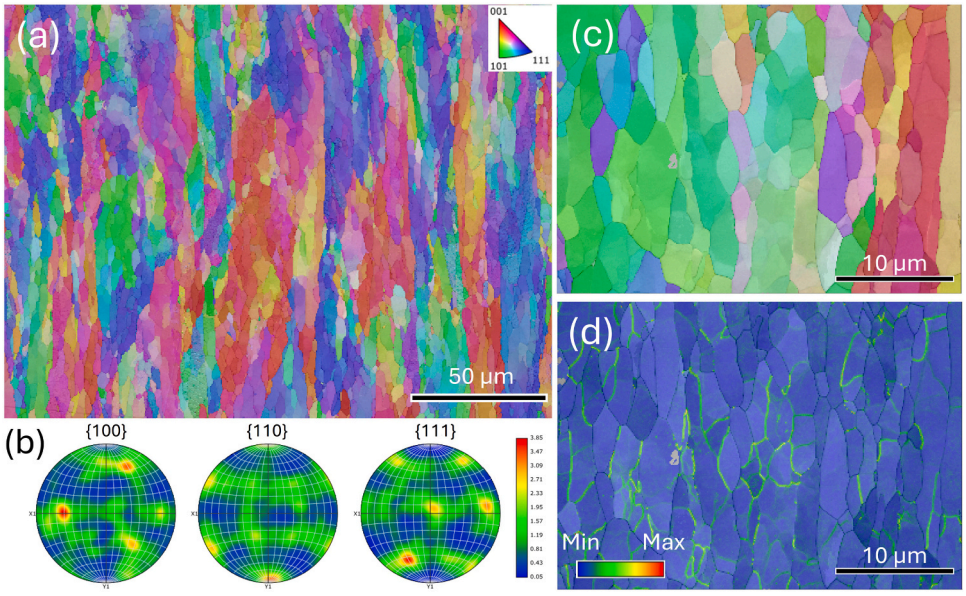

Fig. 2. IPF map and the corresponding pole figure components (a, b), higher magnification of IPF map and GND map (c, d), respectively.

Table 4
The statistical EBSD data for different samples in this study.

	% LAGB (2–5°)	% MAGB (5–15°)	% HAGB (>15°)	GND ($\times 10^{14}$ m^{-2})	Average grain size (μm)
Untreated	14.5	16.2	69.3	6.73	4.54
#S1	38.1	29.8	32.2	32.3	0.63
#S2	43.6	26.1	30.2	36.8	0.6
#S3–1*	25.5	21.3	53.2	37.6	0.5
#S3–2*	30	31.5	38.5	25.1	0.75
#S4	29.3	32.3	34.4	23.4	0.65
#S5	19	18.2	62.8	28.2	0.63
#S6	23	24	53	20.67	0.67
#S7	15.6	19.5	64.9	23	0.51

* #S3–1 and #S3–2 correspond to the top (Fig. 4(b)) and subsurface (Fig. 4(d)) regions of sample #S3, respectively.

3.1.3. *Effect of vibration amplitude*

In order to investigate the influence of vibration amplitude during the UNSM treatment of W, the cross-section of samples #S5 and #S6 are exhibited in Fig. 5. Compared to the sample #S1 (Fig. 3(a-c)), by increasing the vibration amplitude to the 40 μm and 50 μm, respectively in #S5 and #S6 samples, the microstructure of pure W varies significantly during the UNSM treatment. Unlike the #S1 and #S6 samples, the UNSM treatment with an intermediate amplitude of 40 μm deformed homogeneously along the scanning direction, and a deformed layer with an estimated depth of 120 μm in the top surface of the sample #S5 is formed (Fig. 5(a)). Considering the brittle nature of pure W, such a smooth and homogeneous deformation without cracking and de-lamination indicates that the UNSM treatment had the optimum parameters in the sample #S5. The microstructure of the top surface region of the #S5 sample with higher magnification is shown in Fig. 5(b and c). A nano-grained structure with a rough depth of 10 μm was formed in the top surface area as a result of the UNSM treatment (Fig. 5(b)). Beneath this layer, elongated grains formed a fibrous structure and some LAGBs and MAGBs are visible within these grains.

On the other hand, under a greater amplitude value of 50 μm in the #S6 sample, W exhibited a less ductile behavior during the UNSM treatment, and the depth of the deformed layer was around 45 μm, which was significantly shallower than the #S5 sample. In this condition, one can see a similar microstructure and close densities of dislocations, HAGBs, and MAGBs in the samples #S1 and #S6. The periodic behavior of W in terms of the amplitude of the UNSM treatment can be attributed to the dislocation's interactions and the level of dislocation annihilation during the ultrasonic-assisted plastic deformation. It has been well documented that the dislocation annihilation is proportional to the density of acoustic energy [52,53]. While low-amplitude vibrations do not influence dislocation activities, using higher values of ultrasonic amplitude results in the annihilation of dislocations and thus leads to an effective reduction of dislocation densities [54,55]. On the other hand, if the acoustic intensity (proportional to the amplitude) exceeds the specific threshold, which is called the dynamics yield point, ultrasonic waves can activate the dislocation generation sources and lead to dislocation accumulation [56].

Based on those mentioned above, microstructural evolution can be interpreted in the samples #S1, #S5, and #S6 with different amplitudes of 30 μm, 40 μm and 50 μm, respectively. In sample #S1, the induced acoustic energy was insufficient for the comprehensive dislocation annihilation, and the ductile deformation during the UNSM treatment was not enabled due to the high density of dislocations (see Table 4 and Fig. 2(a-c)). On the other hand, using the intermediate amplitude of 40 μm in the sample #S5, the lower dislocation density (see Table 4) through the activation of dislocation annihilation, caused a more pronounced ductile deformation during the UNSM treatment. It should be noted that there is still a high density of dislocations in the sample #S5 (Fig. 5(c)) indicating the competition of two rival mechanisms: (i) dislocation generation as a result of strain hardening, and (ii) acoustic softening due to the dislocation annihilation; however, the overall behavior of the W was a ductile deformation during the UNSM treatment in this sample. According to the EBSD data given in Table 4, the sample #S6 shows a lower density of dislocations compared to the samples #S1 and #S5; however, the microstructure of this sample in Fig. 5(d) does not represent a ductile deformation. This contradiction can be explained through the de-lamination and removal of S^2PD layers during the UNSM treatment like those observed for the #S4 sample in Fig. 4(f-h). It seems that using the greater vibration amplitude (higher acoustic energy) in the #S6 sample led to the activation of dislocation generation sources and the higher density of dislocations resulted in the brittle behavior of W during the UNSM treatment. Therefore, a severe de-lamination occurred, and the S^2PD layers were removed from the beneath layers with lower dislocation density remaining at the top surface of the sample #S6 (Fig. 5(f)).

Such a periodic behavior in terms of vibration amplitude was

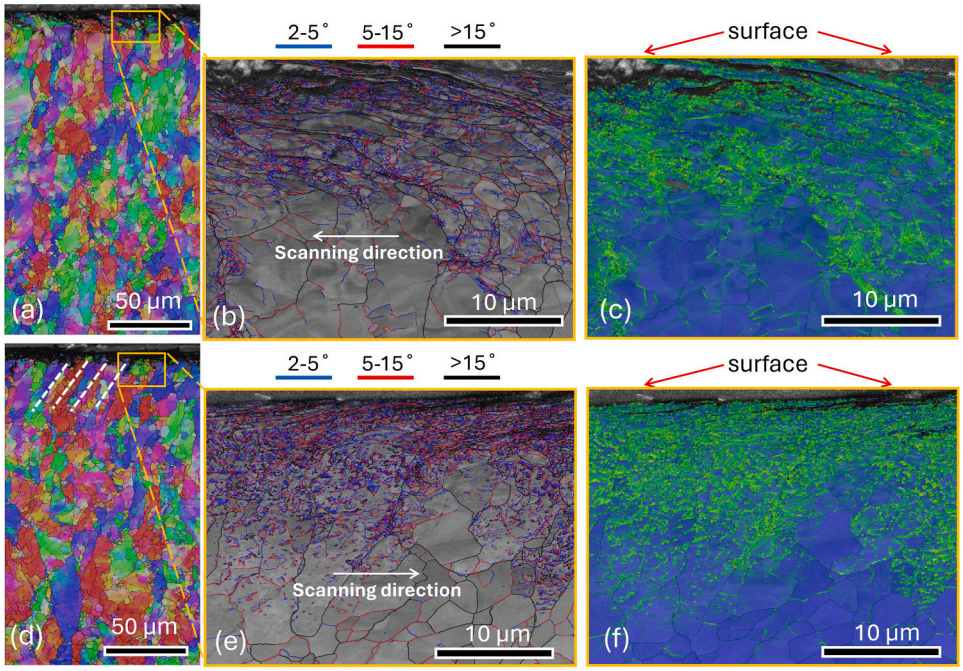

Fig. 3. Cross-sectional EBSD analysis with different magnifications for (a-c) #S1 and (d-f) #S2 samples: (a, d) IPF-x maps, (b, e) pattern quality maps, and (c, f) GND maps.

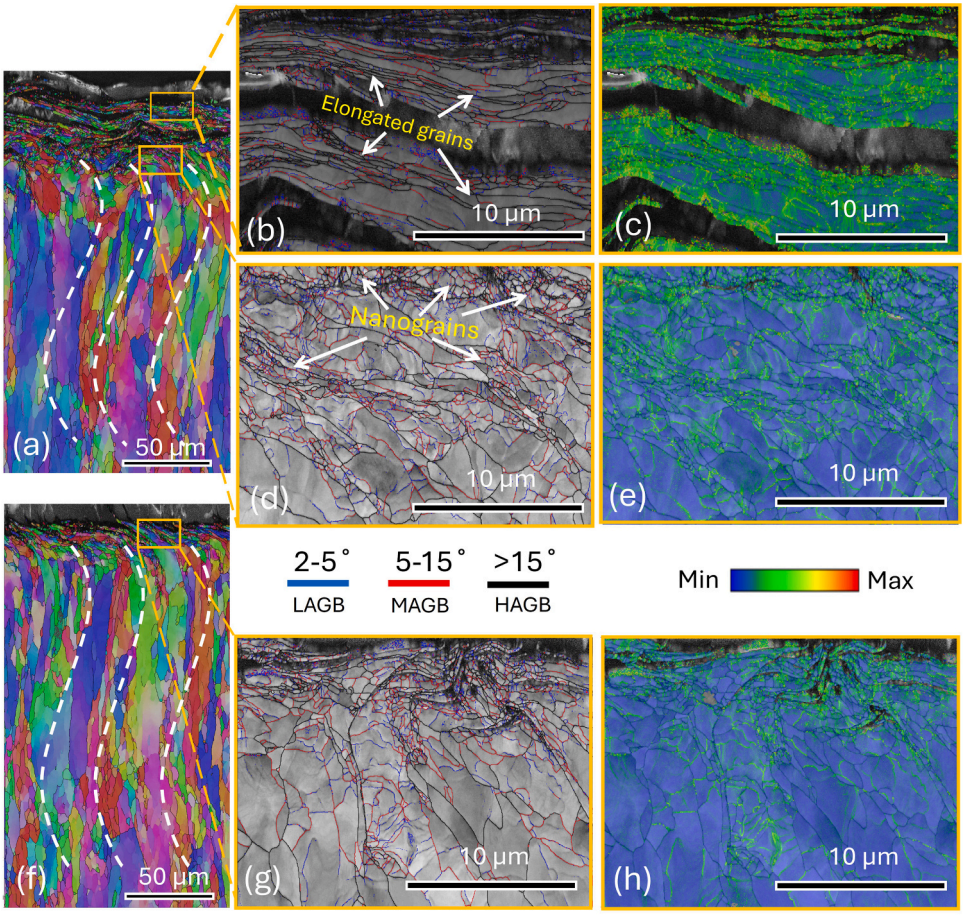

Fig. 4. Cross-sectional EBSD analysis with different magnifications for (a-e) #S3 and (f-h) #S4 samples: (a, f) IPF-x maps, (b, d, g) pattern quality maps, and (c, e, h) GND maps.

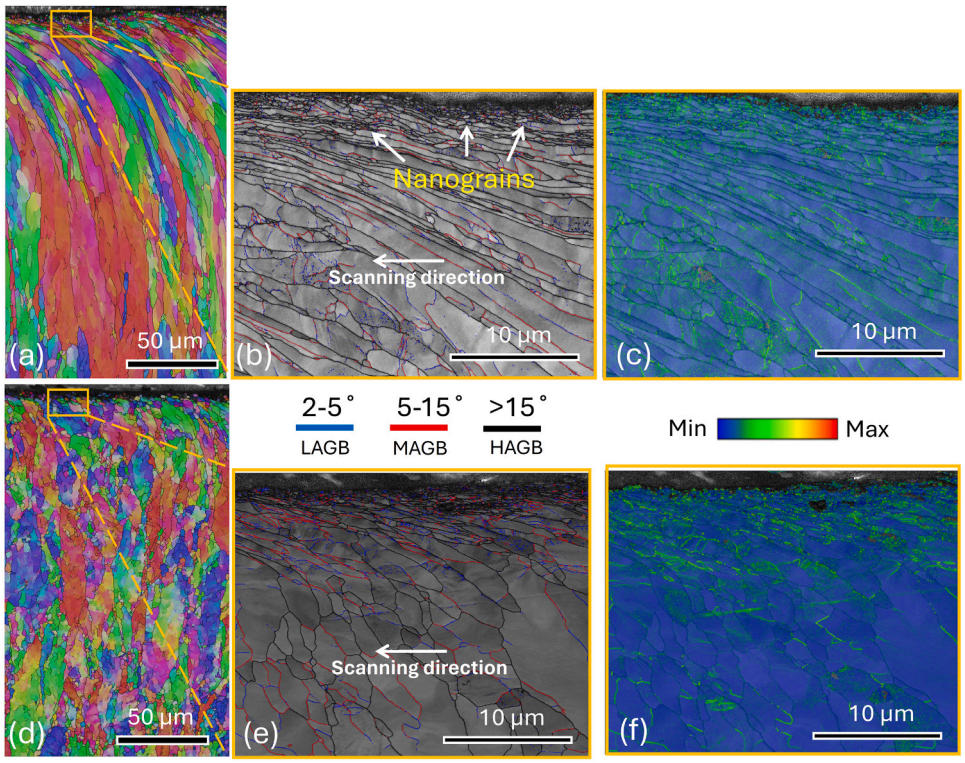

Fig. 5. Cross-sectional EBSD analysis with different magnifications for (a-c) #S5 and (d-f) #S6 samples: (a, d) IPF-x maps, (b, e) pattern quality maps, and (c, f) GND maps.

reported by other researchers [57]. For instance, Samigullina et al. [12] investigated the ultrasonic treatment of severely deformed nickel and showed that there is an intermediate optimum vibration amplitude in which the density of dislocations within the UFGs is minimized and the material has the minimum internal energy. In another research on the ultrasonic treatment of duplex stainless steel, it has been reported that enhanced ductility can be achieved by using the optimum amplitude [58].

3.1.4. *Grain refinement mechanism*

According to the EBSD data provided in Table 4, the UNSM treatment resulted in remarkable grain refinement in W. The average grain size was decreased from 4.5 μm in the untreated sample to less than 0.7 μm in the UNSM-treated samples. Investigating the possible mechanisms for such significant grain refinement is also important, as it can help to achieve the optimum UNSM treatment parameters for advanced properties. For this purpose, the cross-sectional EBSD analysis of the sample

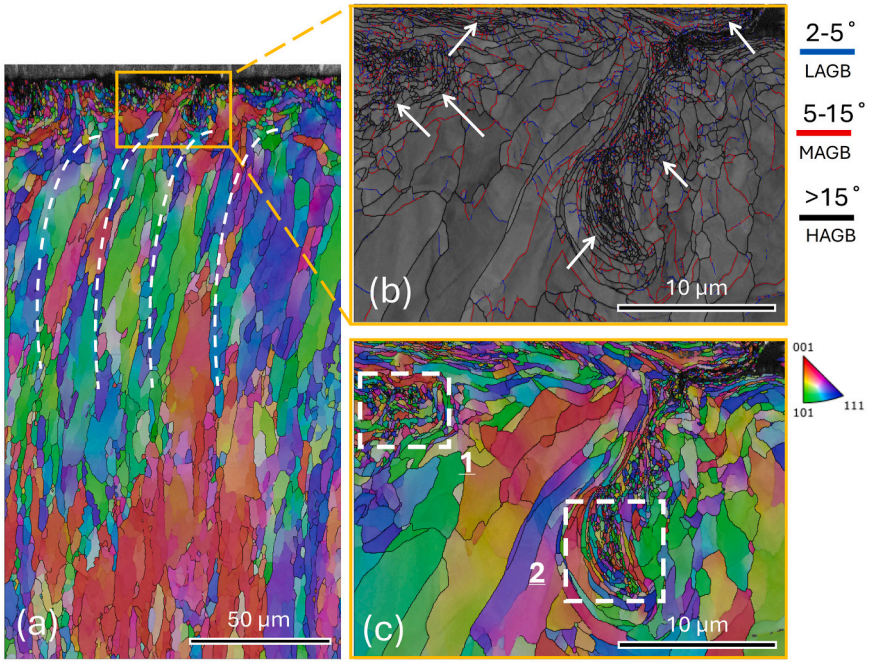

Fig. 6. Cross-sectional EBSD analysis with different magnifications for the sample #S7: (a, c) IPF-x maps, (b) pattern quality map.

#S7 is presented in Fig. 6. As discussed in sub-Section 3.1.2, pure W represents a ductile behavior using the intermediate vibration amplitudes. Through the UNSM cross-scanning under this condition, a wavy configuration with an estimated depth of 100 μm was formed in the sample #S7 (Fig. 6(a)). It is essential to mention here that the nanostructures at the top surface layer retain columnar structures, which is important for fusion (see Fig. 6(a)). At higher magnifications, a unique vortex structure is visible at the top surface region. As highlighted by arrows in Fig. 6(b), grains within the vortex structure as well as those around the top surface are nano-scaled and a UFG region can also be seen around the nano-structured area. While the average grain size of the sample #S7 is given as 0.51 μm in Table 4, the grain size in regions 1 and 2 in Fig. 6(c) (vortex structure areas) are 0.34 μm and 0.39 μm, respectively. Considering Fig. 6(b and c), nanograins mainly posed HAGBs and formed a random texture, which both are the characteristics of recrystallized grains. The vortex structure seems to be formed as a result of collision, rotation, and rolling over of grain layers during the cross-UNSM scanning, which was perpendicular to the direction of the first scan. Such an S^2PD can provide accumulated strain, which is the required activation energy for recrystallization. On the other hand, observation of LAGBs and MAGBs close to the nanograined regions can be regarded as occurring in the recovery process.

In order to verify the assumption of the occurrence of recovery and recrystallization and explore the grain refinement mechanism, the statistical EBSD data needs to be evaluated. According to Table 4, there are correlations among variations in the grain size, fraction of grain boundaries, and dislocation densities of the samples. Almost all samples after UNSM treatment exhibit higher dislocation densities, LAGB, and MAGB fractions, but lower HAGBs and grain sizes compared to the untreated sample. In the samples #S1 and #S2 with maximum LAGBs fractions of 38 % and 43 %, it seems that polygonization of dislocations into the low-angle grain sub-boundaries has been the dominant mechanism during the UNSM treatment. With double UNSM treatment in the samples #S3 (#S3–2) and #S4, the misorientation angle of grain sub-boundaries increased and LAGBs gradually evolved to MAGBs. The maximum fraction of MAGBs and the lower fraction of LAGBs compared to the samples #S1 and #S2 suggest the domination of dynamic recovery in the samples #S3 (#S3–2) and #S4. It is worth mentioning here that the grain size was slightly increased during the dynamic recovery process, which can be attributed to the limited migration of grain sub-boundaries due to the interaction with lattice dislocations. The maximum density of dislocations and a lower fraction of LAGBs in the #S3–1 sample imply that the top surface layers were delaminated before activation of the dislocation polygonization and dynamic recovery mechanisms. Likewise, in the #S5 sample, due to the dislocation annihilation and lower density of dislocations, the recovery mechanisms were not complete and a lower fraction of LAGBs and MAGBs were formed. Eventually, in the #S7 sample due to the most S^2PD and greater stored strain energies, the dynamic recrystallization was activated during the cross-UNSM treatment and the minimized grain size, LAGBs, and dislocation density as well as maximum HAGBs, like the untreated material, implying a well-developed recrystallization, especially at the top surface area and vortex regions with maximum stored strain. Based on the above-mentioned mechanisms, the grain refinement steps can be summarized as the schematic illustration in Fig. 7. According to the suggested mechanisms, the grain refinement during the UNSM treatment of W includes four main steps of cold deformation, dislocation polygonization, dynamic recovery, and dynamic recrystallization. A similar grain refinement mechanism has been reported for W during the SMAT [39,40], grinding and subsequent annealing [41], and explosive deformation [59].

Texture analysis is another way, which can be employed for investigating microstructural evolution and dominant mechanisms. For this purpose, the inverse pole figures of the samples are presented in Fig. 8, and the analyzed textures are summarized in Table 5. The untreated sample exhibits a more random texture with the maximum intensity of $< 111 > ||$SD (scanning direction is equal to rolling direction). Following the UNSM treatment, the intensity of $< 111 > ||$SD component decreased significantly. In addition, the $< 110 > ||$SD component, which is known as rolling texture in BCC metals [60], was intensified after the UNSM treatment. The rolling texture especially in the samples #S3 and #S4 due to the multiple scanning, and in the samples #S5 and #S6 because of higher acoustic energy was the dominant texture. On the other hand, the $< 110 > ||$SD component in the sample #S7 is weakened significantly, and increasing the intensity of $< 111 > ||$SD and $< 100 > ||$SD components provided a more random texture similar to the untreated sample. These observations support the previous discussion on the activation of the recrystallization mechanism in sample #S7.

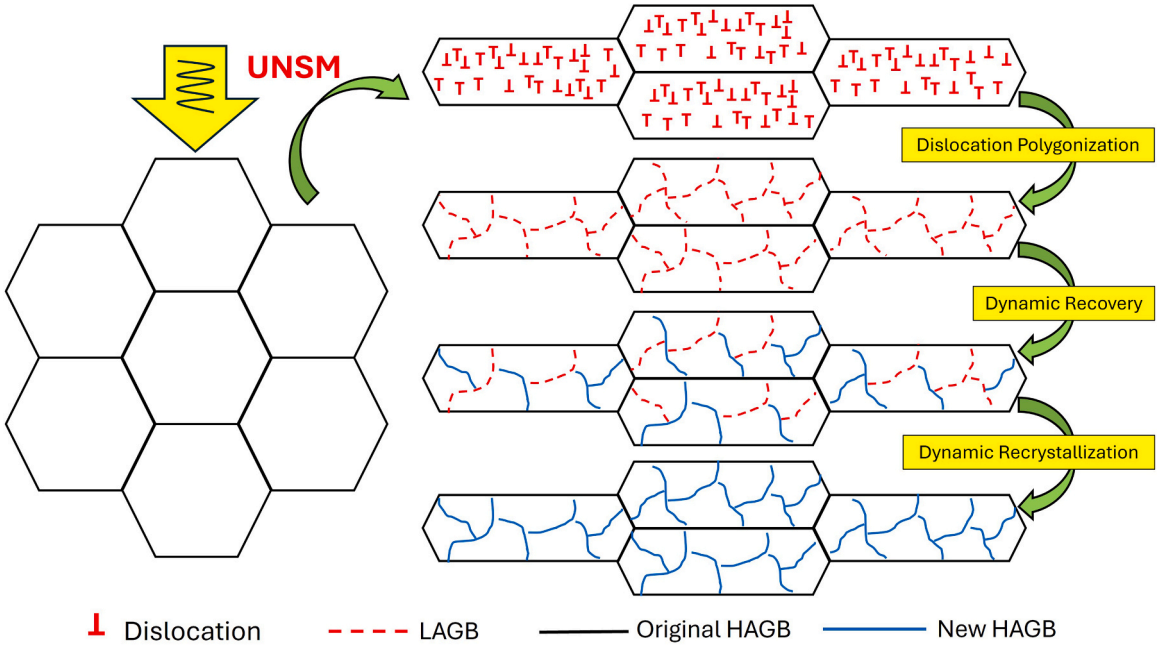

Fig. 7. Schematic illustration of grain refinement mechanisms during the UNSM treatment.

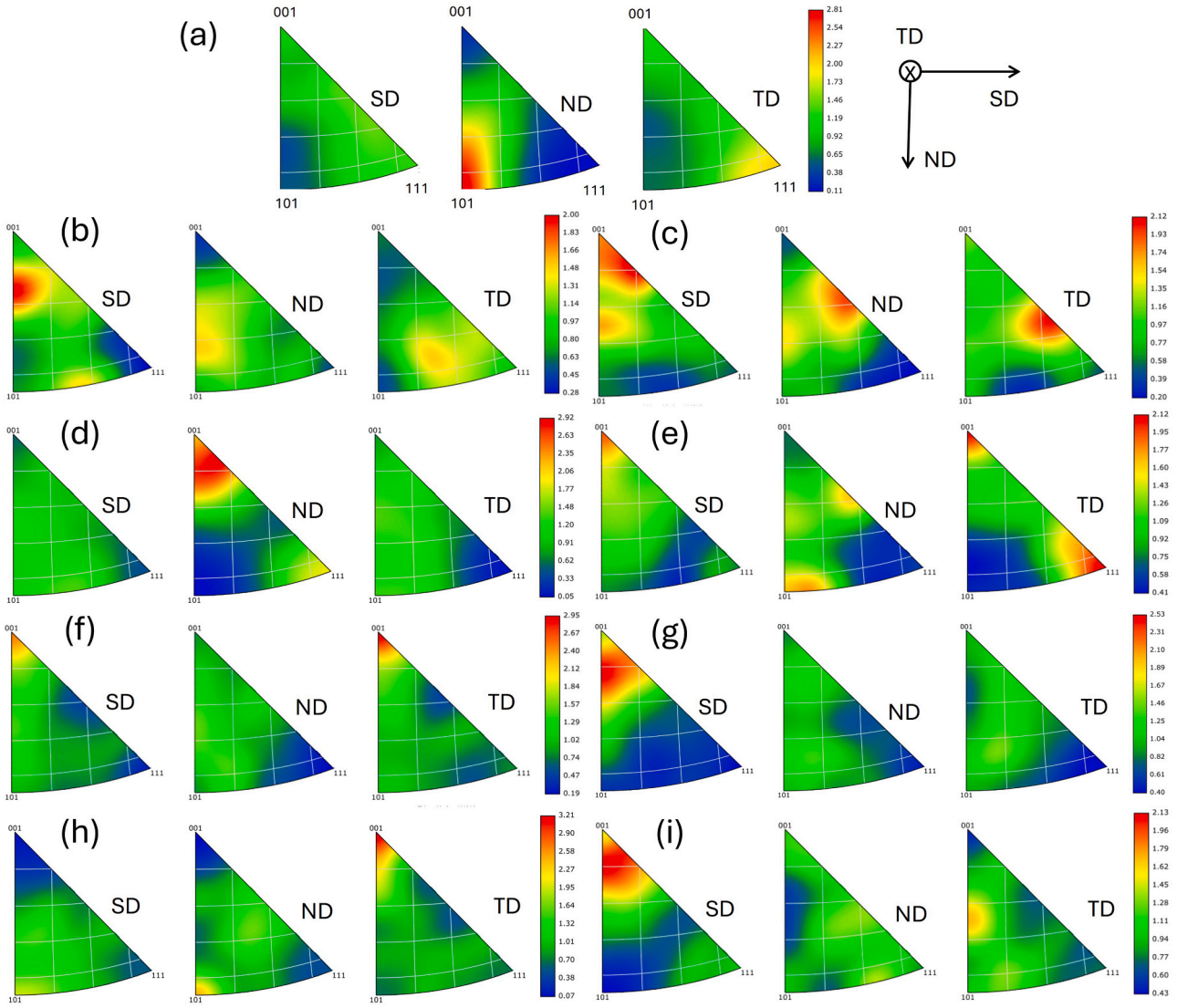

Fig. 8. The IFP texture components along scanning direction (SD), normal direction (ND), and transverse direction (TD) for different samples: as-received (a), #S1 (b), #S2 (c), #S3–1 (d) (top region), #S3–2 (beneath region) (e), #S4 (f), #S5 (g), #S6 (h), #S7 (i).

Table 5
Area fraction of the main texture components for different samples in this study.

	< 111 > //SD (%)	< 110 > //SD (%)	< 001 > //SD (%)
Untreated	27	22.6	17.9
#S1	14	25.6	31.2
#S2	13.9	29.8	28
*#S3–1**	16	39.7	16.7
*#S3–2**	14.1	32.2	24.6
#S4	16	36	28.2
#S5	18	50.2	8.02
#S6	10.8	37.6	22.3
#S7	18.5	21.2	35.3

* #S3–1 and #S3–2 correspond to the top layers (Fig. 4(b)) and subsurface region (Fig. 4(d)) of sample #S3, respectively.

3.2. Hardness and residual stress

The effect of the UNSM treatment with different parameters in the samples #S1 (reference condition) and #S5 (optimized condition) on microhardness, residual stress, and the full width at half maximum (FWHM) XRD peak values are compared with the untreated sample and results are plotted as shown in Fig. 9. The surface hardness of the untreated sample after the UNSM treatment was increased significantly by 31 % for the sample #S1, and by increasing the vibration amplitude in the sample #S5, it was reduced slightly to 567 HV. The increase in the surface hardness can be attributed to grain refinement and the increase in the dislocation density, caused by S^2PD through the UNSM treatment. On the other hand, a reduction in surface hardness in the sample #S5 can be related to its lower dislocation density than the sample #S1, as reported in Table 4. Based on the measured residual stress in Fig. 9, the UNSM treatment led to relieving the tensile residual stress of 400 MPa and induced a beneficial compressive residual stress in the top surface of the material. It can be seen that the homogeneous deformation with higher depth in the sample #S5, resulted in a greater compressive residual stress compared to the sample #S1 with a shallower deformation layer (see Fig. 3(a) and 5 (a)). Fig. 9 also shows that the UNSM treatment resulted in the XRD peak broadening and an increase in the FWHM values, which can be attributed to the lattice distortion and reducing the crystalline size as a result of S^2PD. Similar effects of the UNSM treatment on increasing the surface hardness and FWHM values and the introduction of the compressive residual stress have been reported for a wide range of materials [61,62]. Moreover, the observed trend in the present work is similar to the reported results for W by other surface treatment processes like SMAT [39,40] and LSP [47].

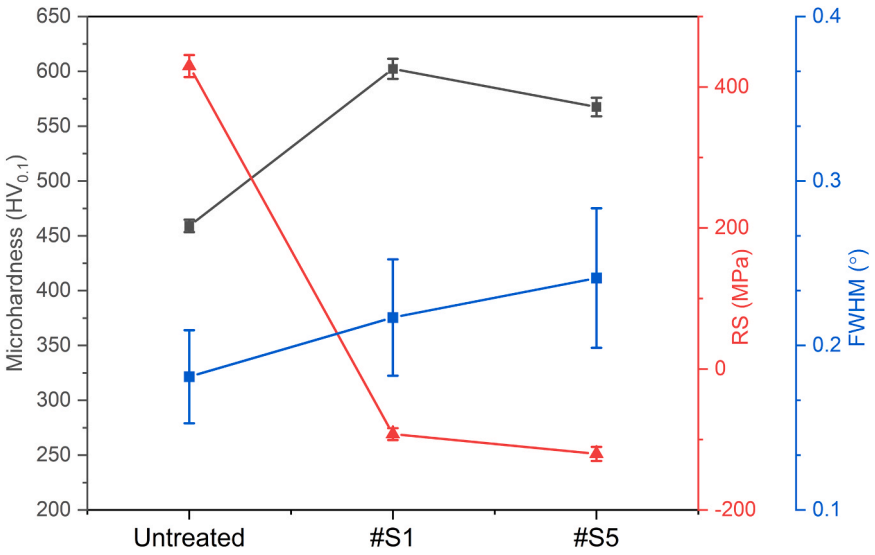

Fig. 9. Variation of microhardness, residual stress, and FWHM values for the untreated, #S1, and #S5 samples (error bars represent the standard deviation).

3.3. Tribological properties

3.3.1. Coefficient of friction and wear resistance

Fig. 10 shows the dry frictional behavior of the untreated and UNSM-treated #S1 (reference condition) and #S5 (optimized condition) samples as a function of sliding time against a stainless steel 440 counterface ball. It is obvious that the COF of the untreated sample increased at the beginning of the test and reached a COF value of about 0.41. With continuing the reciprocating sliding, the COF gradually increased, where it reached a COF of 0.62 at the end of the reciprocating sliding test. It was confirmed from the frictional behavior of the UNSM-treated samples that both samples (#S1 and #S5) had two distinct running-in and steady-state phases. It can be noticed that the running-in period of the UNSM-treated samples was close, but the COF of the sample #S5 with optimized UNSM parameters was lower than the reference sample #S1. The UNSM-treated samples #S1 and #S5 demonstrated a stable COF of about 0.50 and 0.42 in the steady-state phase throughout the tribological testing of 10 min of reciprocating sliding, respectively. This can be associated with the change in surface roughness after UNSM treatment, where the running-in period is the initial phase of friction during the interaction of the highest asperities of the surfaces leading to lesser contact resistance due to a change in the true contact area at the interface between the sample and the counterface ball. In other words, as the samples started wearing out, the surface was smoothed resulting in a reduction in surface roughness due to the complete formation of blunt asperities and less wear debris generation at the contact interface during the reciprocating sliding. However, it seems for the untreated sample that the surface asperities were not completely worn out until the reciprocating sliding time of 10 mins resulting in the generation of wear debris at the contact interface. These surface smoothing and wear debris generation phenomena can be confirmed by different levels of fluctuations for the untreated and UNSM-treated samples, where the sample #S5 had the lowest fluctuation of frictional behavior. A stable frictional behavior with a relatively low COF of the UNSM-treated sample is of

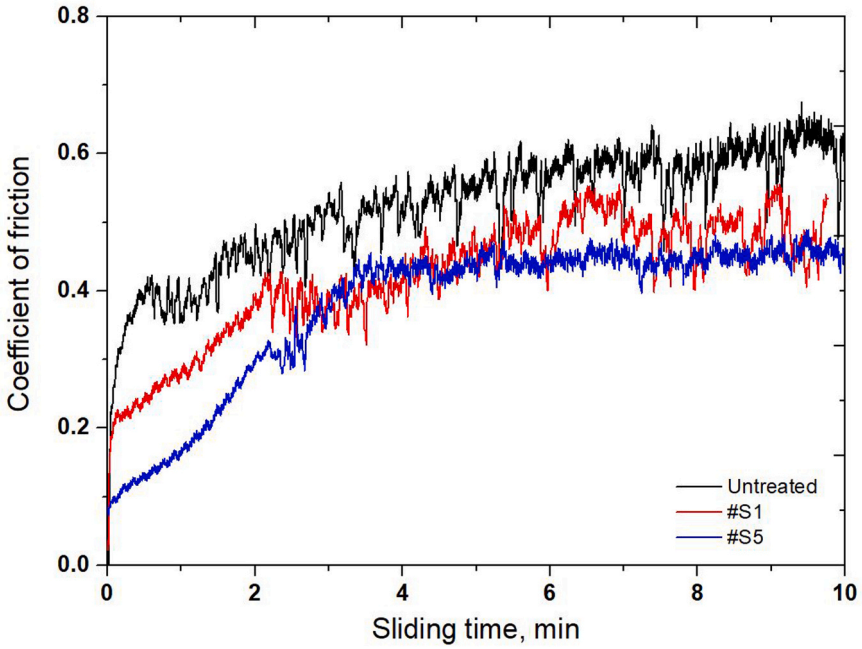

Fig. 10. Frictional behavior of the untreated and UNSM-treated samples.

interest to enhance the performance and extend the service life of components by increasing the mechanical properties and wear resistance. It was confirmed that there is a possibility of controlling the COF to achieve a stable frictional behavior, which may lead to various benefits, including improved energy efficiency, component longevity, and contribution to smoother operation. It is believed that the dominant factor in controlling the frictional behavior of W is the change in surface roughness after UNSM treatment, but for sure the increased mechanical properties, especially surface hardness and compressive residual stress shown in Fig. 9 are also important factors to be considered: lower surface roughness after UNSM treatment under dry conditions generally has many effects: smoother surfaces tend to reduce the COF because there are fewer asperities (peaks and valleys) to cause mechanical interlocking between surfaces in contact which may lead to a lower friction force. With fewer asperities, the real area of contact (the points where the two surfaces touch) is reduced, which diminishes the resistance to sliding. However, this is more noticeable at lower loads; at higher loads, even smoother surfaces can deform, increasing contact area and possibly increasing friction. Higher surface hardness has also significant effects on both the COF and wear resistance of the UNSM treated sample under dry conditions. For example, a harder surface is less likely to deform under load, which reduces the real area of contact between the two surfaces. As a result, the friction coefficient may be reduced because there is less interlocking deformation between the mating surfaces. It also tends to have lower adhesive forces at asperity junctions, which are points where surface peaks make contact. This reduction in adhesion further contributes to a lower friction coefficient, especially under dry conditions. Higher compressive residual stress in a material can have notable effects on the COF, particularly under dry conditions. For example, compressive residual stress tends to inhibit surface roughness from deforming or breaking down during sliding contact, leading to less mechanical interlocking between surfaces. This may result in a lower COF since the surfaces can glide more easily over each other. However, it is worth mentioning that the effect of compressive residual stress on the COF is usually minor compared to its impact on wear resistance. It is worth mentioning that Jiang et al. reported a running-in stage and also stable COF with a value of 0.5 for the untreated W against an Al_2O_3 counterface ball under dry conditions [45]. Again, the same authors with the same tribo pair pointed out that a high fluctuation in the frictional behavior occurred due to the roughness variation of the W samples [43]. Furthermore, Ding et al. also reported that the COF of the W against an Al_2O_3 counterface ball at room temperature under dry conditions was 0.45 [46].

Fig. 11 shows the 3D images of the wear tracks and their cross-sectional profiles for the untreated and UNSM-treated samples. It seems from these 3D images that the UNSM treatment remarkably increased the wear resistance of the untreated sample (see Fig. 11 (a)) regardless of UNSM treatment parameters. The exact cross-sectional wear track profiles were obtained to calculate the SWR of the samples. It is confirmed from the cross-sectional profiles that the UNSM treatment had significantly shallower and narrower wear track profiles (see Fig. 11 (b and c)) compared to that of the untreated sample, where the influence of the sample #S5 was more pronounced than that of the sample #S1. This means that the UNSM treatment with optimized conditions demonstrated a more beneficial influence on the wear resistance of the sample than the UNSM treatment with reference conditions thanks to the difference in surface roughness, higher compressive residual stress, and higher depth of deformed layer. Fig. 11 also shows the cross-sectional profiles of the untreated and UNSM-treated samples in a longitudinal (X-axis) direction (Fig. 11 (d)) and in a transverse (Y-axis) direction (Fig. 11 (e)), respectively. It is clear that the width and depth of the wear track formed on the surface of the untreated sample were wider and deeper than those of the wear track formed on the surface of the UNSM-treated samples. It was observed that pileups on both sides of the wear tracks were generated at different heights due to the pushing effect of the counterface that accumulated the wear debris and formed an oxide layer on the surface of the wear track. The calculated SWR of the untreated, UNSM-treated #S1 and UNSM-treated #S5 samples was 0.0106 $mm^3/N \times m$, 0.007526 $mm^3/N \times m$ and 0.006572 $mm^3/N \times m$, respectively. It can be concluded according to the calculated SWR of the samples that the UNSM treatment with reference (#S1) and optimized (#S5) conditions increased the wear resistance of the untreated sample by about 29 % and 38 %, respectively. The obvious correlation between the friction coefficient and wear behavior was observed, where the lower the friction coefficient the higher the wear resistance. The increase in wear resistance of the untreated sample by UNSM treatment is associated with changes in surface roughness, surface hardness, and compressive residual stress. It is well-known that

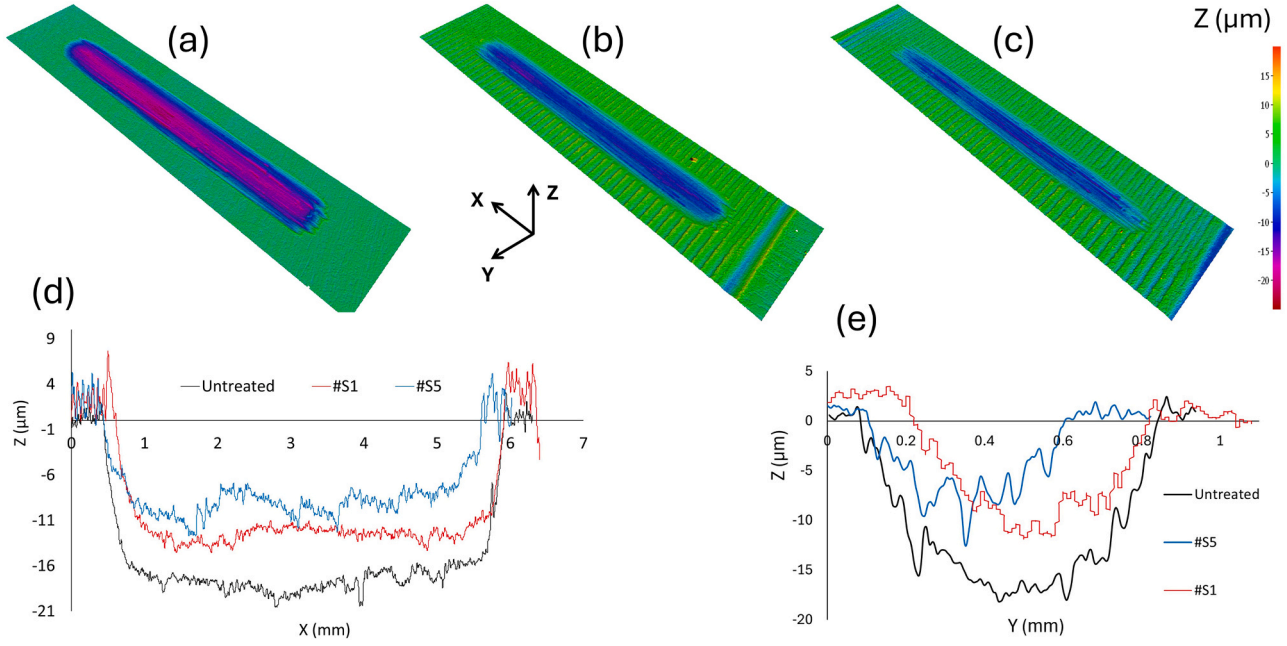

Fig. 11. 3D images of the wear tracks for the untreated (a) and UNSM-treated #S1 (b) and #S5 (c) samples. Corresponding cross-sectional profiles along the X-axis (d) and Y-axis (e).

UNSM-induced surface roughness usually leads to improved wear resistance because smoother surfaces experience less abrasive and adhesive wear under dry conditions. Higher hardness improves wear resistance because harder materials are more resistant to plastic deformation, cutting, and material removal. Under dry reciprocating sliding conditions, where wear occurs primarily due to mechanical abrasion or adhesion, a harder surface is better able to withstand these forces. In the case of higher compressive residual stress, it tends to increase the load-carrying capacity of the surface. This makes the material more resistant to plastic deformation, thereby reducing the likelihood of material being removed during sliding under dry conditions. It also improves resistance to surface fatigue, which can cause material loss over time, especially under dry conditions, where there is no lubrication to alleviate stress.

3.3.2. *Wear mechanisms*

When pure W and stainless steel 440 interact under dry sliding conditions, the wear mechanisms are influenced by the material properties of both materials. In this study, the wear mechanisms of the two different mated materials were investigated by characterizing the worn-out surface of the wear track formed on the surface of the untreated and UNSM-treated samples and the counterface ball that came into contact with the samples. It is worth mentioning that commercially available balls made of stainless steel 440 without surface treatment were used in this study. Fig. 12 shows the SEM images of the wear track at various magnifications after the reciprocating sliding test under dry conditions. As shown in Fig. 12 (a1), the counterface ball abraded the pure W surface creating grooves and scratches, which indicated a significant abrasive wear mechanism. The width of the wear track was about 765 μm in the untreated sample, as shown in Fig. 12 (a2). At higher magnification of the SEM image (Fig. 12 (a3)), severe material degradation and plastic deformation with an uneven and rough surface texture were observed. The deep grooves suggest that abrasive wear is the primary wear mechanism likely from hard particles and asperities sliding along the surface and creating parallel scratches on the worn-out surface. It is obvious by the highest magnification of the SEM image (Fig. 12 (a4)) that the surface was plastically deformed confirming the signs of wear-induced material flow and detachment. These occurred due to the high contact pressure, which caused the untreated pure W to yield. Jiang et al. and Ding et al. studied the wear mechanisms of W against an Al_2O_3 counterface ball under dry conditions at room and high temperatures [45,46]. Both concluded that the main wear mechanisms at room temperature were abrasive, adhesive, and fatigue due to the brittleness of W. As shown in Fig. 12 (b1), the counterface ball abraded the surface of the #S1 sample creating grooves and scratches, which were less pronounced than in the untreated sample suggesting a reduction in abrasive wear. It is clear from Fig. 12 (b2) that the width of the wear track for the #S1 sample was about 620 μm indicating reduced material removal of about 19 % compared to the untreated sample. At

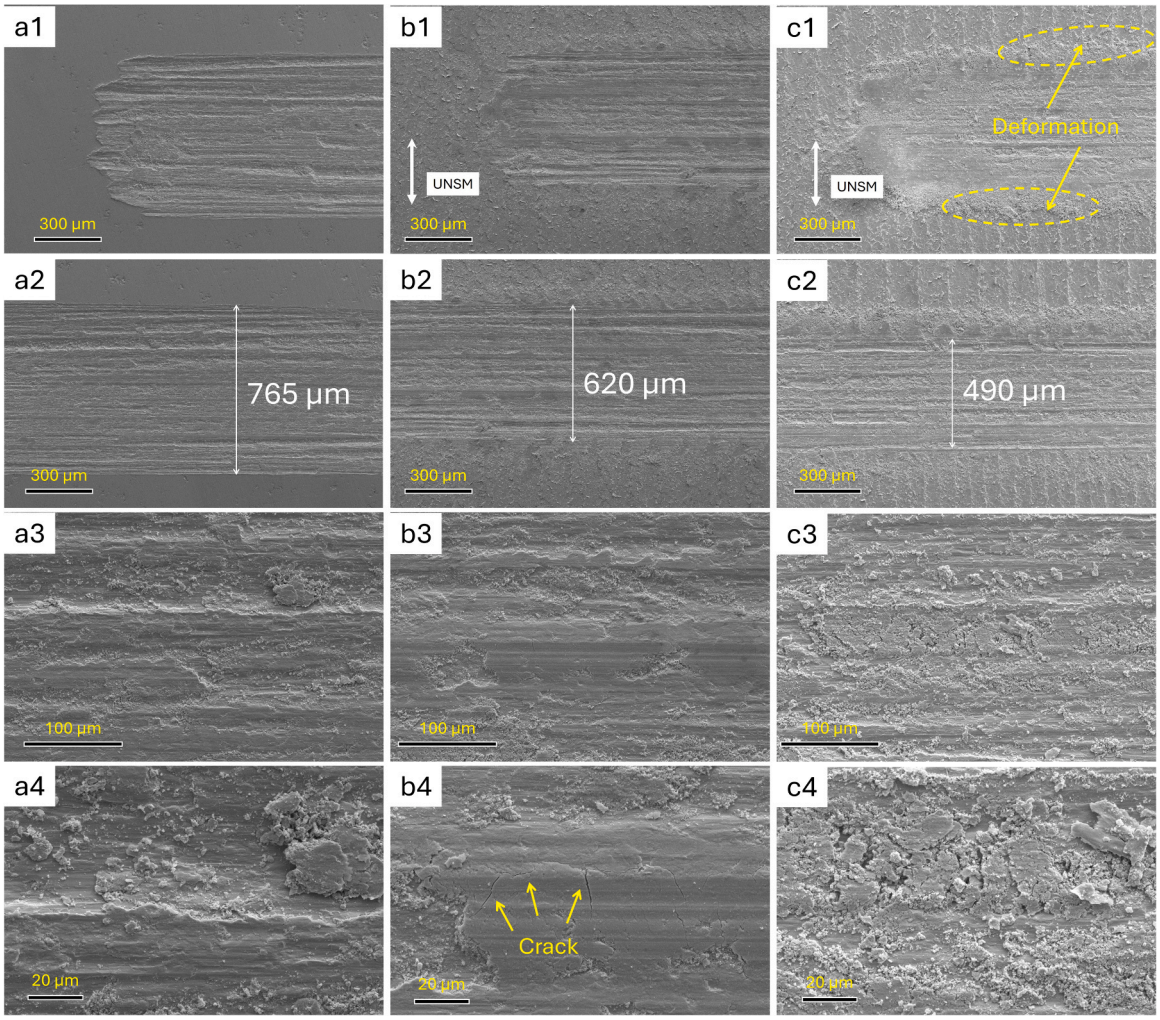

Fig. 12. Low- and high-magnification SEM images of the wear track generated on the surface of the untreated (a) and UNSM-treated #S1 (b) and #S5 (c) samples. Figures (a1-c1) and (a2-c2) correspond to the wear tracks edge and center, respectively. The higher magnifications images (a3-c3) and (a4-c4) were taken from the wear tracks center region.

higher magnification of the SEM image (Fig. 12 (b3)), relatively less material degradation and plastic deformation with an uneven and rough surface texture were also observed. The relatively deep grooves suggest that abrasive wear is the primary wear mechanism. The highest magnification of the SEM image (Fig. 12(b4)) confirmed that the microcracks indicated surface fatigue wear, where the contact stress has caused the micro-crack initiation and further propagation. There is less evidence of plastic deformation, likely due to the UNSM treatment increasing the surface hardness and resistance to plastic flow. For the sample #S5 with optimized UNSM parameters, Fig. 12 (c1) shows the least wear with the shallowest grooves and minimal visible damage compared to the untreated and UNSM-treated #S1 samples. It suggests that the surface has a high wear resistance, likely due to a deeper deformed layer in the sample #S5 (see Fig. 3(a) and 5 (a)). In addition, abrasive wear and plastic deformation are significantly reduced compared to the untreated and single UNSM-treated samples. The deformation of the edge of the wear track, as shown in Fig. 12 (c1), indicated minor localized plastic deformation. It is clear from Fig. 12(c2) that the width of the wear track was about 490 μm indicating the least reduced material removal of about 36 % and 21 % compared to the untreated and #S1 samples. At higher magnification of the SEM image (see Fig. 12 (c3)), the surface of the wear track is relatively rough, but it has fewer cracks and signs of severe wear compared to the untreated and #S1 samples. The highest magnification of the SEM image (see Fig. 12 (c4)) showed a smeared wear particle on the surface of the wear track. In conclusion, the untreated pure W against a stainless steel 440 ball under dry conditions, severe wear with significant abrasive wear and surface deformation mechanisms dominated. The UNSM treatment with reference conditions demonstrated moderate wear with signs of abrasive wear, cracking, and reduced plastic deformation. The UNSM-treated sample with optimized conditions showed the least wear with abrasive wear being supplemented by minimal oxidative wear. It was confirmed that the UNSM treatment seemed to have reduced the overall wear severity compared to the untreated sample.

Fig. 13 shows SEM-EDS analysis of wear tracks generated on the surface of the untreated and UNSM-treated samples under dry sliding conditions. Fig. 13 (a1, b1, and c1) presents the backscattered electron (BSE) images showing the morphology of the wear tracks discussed previously. Fig. 13 (a3, b3, c3, and d3) depicts the oxygen map demonstrating a low presence of oxygen across the wear track, suggesting minimal oxidative wear, while the #S1 sample exhibited a bit higher oxygen compared to the untreated and #S5 samples. It is worth pointing out that in the case of the sample #S1, there was a moderate increase in oxygen signal along the wear track, suggesting that oxidative wear is beginning to contribute. The presence of oxygen could indicate the formation of an oxide layer, which might provide some protective effect and help reduce wear. The absence of a significant oxygen signal indicates that oxidation likely did not play a major role in the wear mechanisms for the interaction of W against a stainless steel 440 interaction under dry conditions. Fig. 13 (a4, b4, c4, and d4) presents the Fe map showing a uniform presence of Fe along the wear track. This is expected because Fe is likely transferred from the counterface ball made of stainless steel 440. The atomic percent ratio of oxygen to tungsten (O/W) for the wear tracks was obtained as 0.44, 0.41 and 0.34 for the untreated, S1 and #S5 samples, respectively.

Fig. 14 presents the SEM images of the wear scar (W transfer) generated on the surface of the counterface ball. As shown in Fig. 14 (a1), The wear scar on the surface of the counterface ball appears quite large with rough and uneven morphology, which indicates significant material deformation and transfer in the untreated sample. Fig. 14 (a2) shows a closer observation, which indicated noticeable wear debris and grooves along the sliding reciprocating direction. This suggests abrasive wear due to the hard stainless steel counterface, which likely caused micro-cutting or plowing of the softer pure W sample. Severe roughness within the wear scar, with substantial debris and fragmented material visible is shown in Fig. 14 (a3). These particles are likely to wear debris, indicating that adhesive wear or material transfer might also be contributing to the wear mechanism, alongside abrasion. As shown in Fig. 14 (b1), the wear scar generated on the surface of the counterface ball reciprocated against the #S1 sample appeared somewhat reduced compared to the untreated sample, suggesting that the UNSM treatment with reference conditions has had a positive effect on wear resistance. At

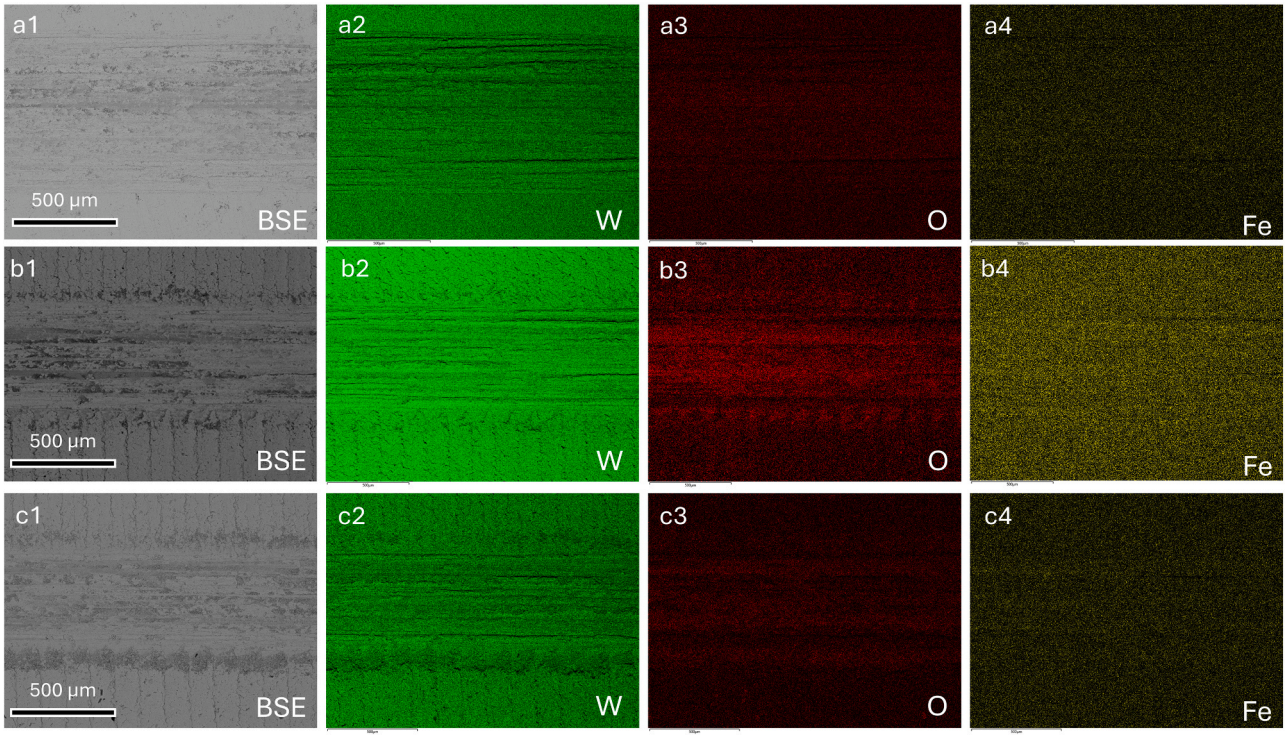

Fig. 13. SEM-EDS images of wear tracks generated on the surface of the untreated (a) UNSM-treated #S1 (b) and #S5 (c) samples.

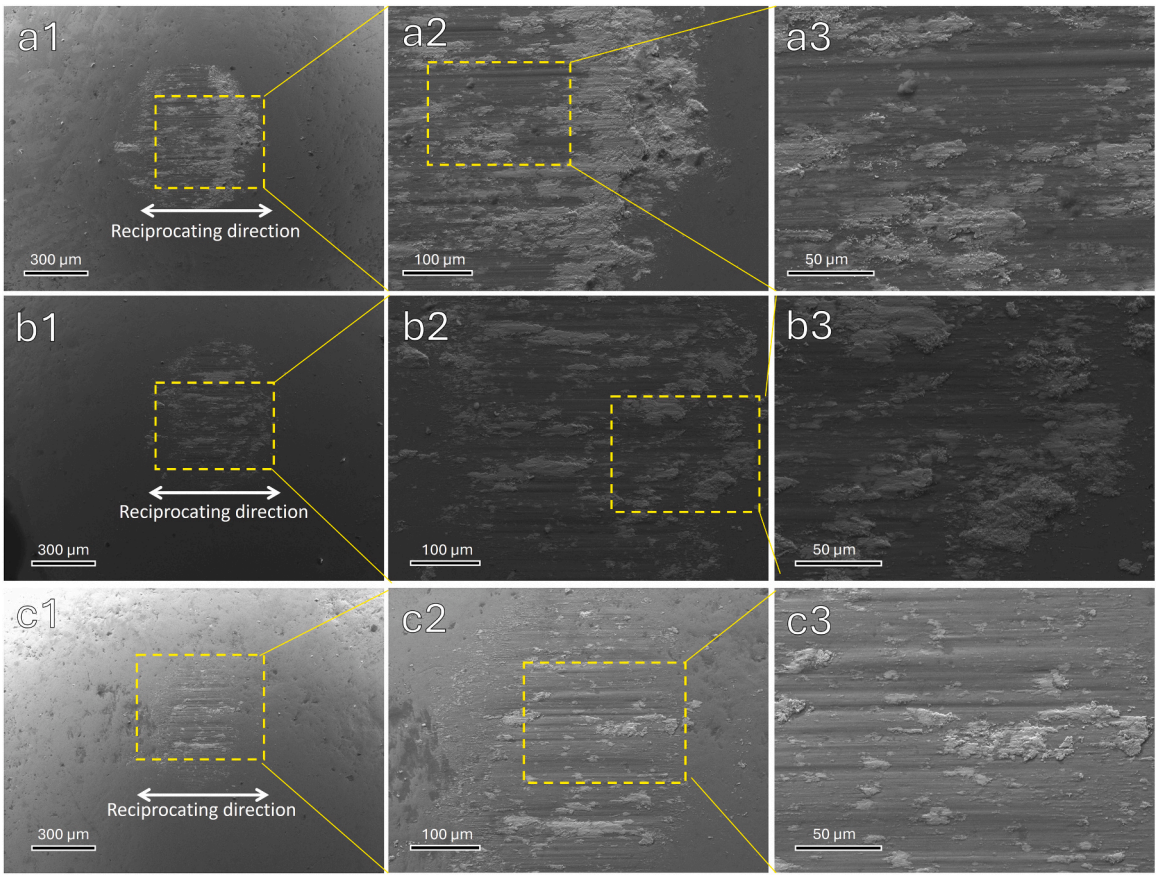

Fig. 14. Low- and high-magnification SEM images of the wear scar generated on the surface of the counterface ball came into contact with the untreated (a) and UNSM-treated #S1 (b) and #S5 (c) samples.

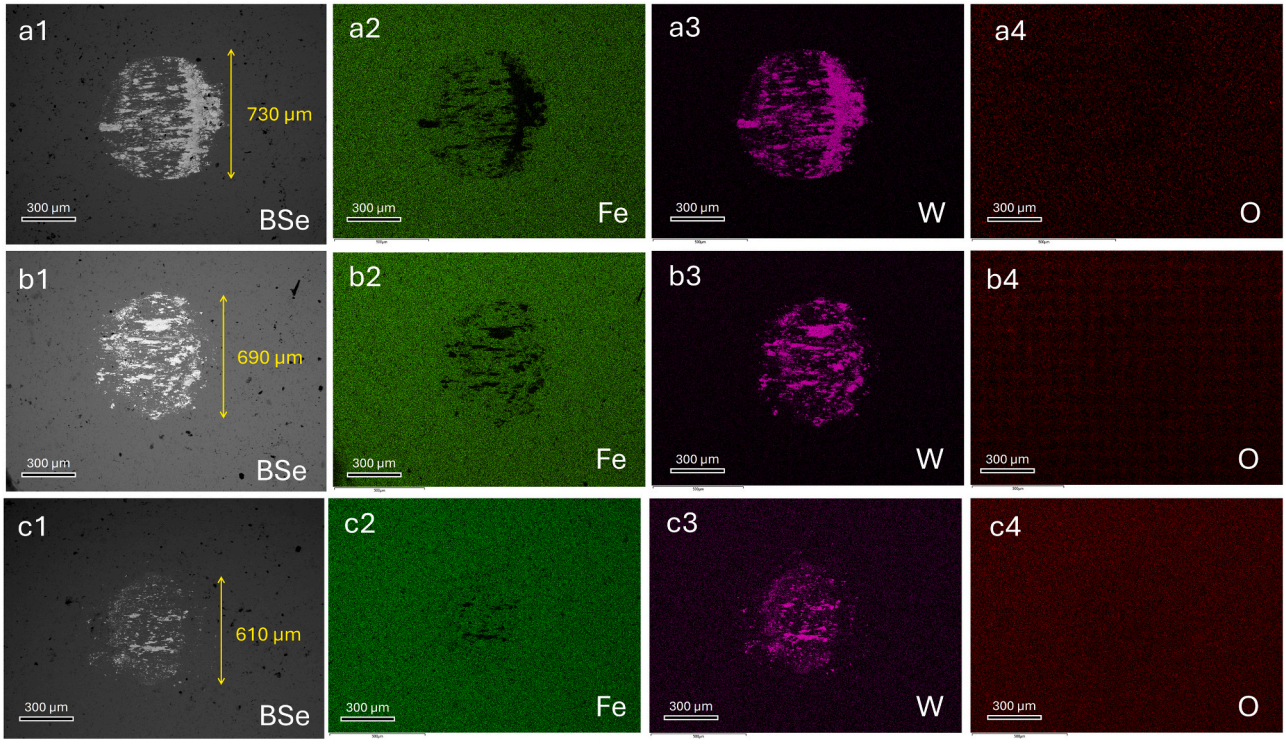

Fig. 15. SEM-EDS images of the wear scar generated on the surface of the counterface ball that came into contact with the untreated (a), UNSM-treated #S1 (b) and #S5 (c) samples.

a higher magnification shown in Fig. 14 (b2), the wear scar is still evident, but with a smoother appearance compared to the untreated sample. This indicates less severe abrasive wear, which may be due to the increased hardness and formed nanostructured surface layer resulting from the UNSM treatment. At the highest magnification (see Fig. 14 (b3)), smaller debris particles are visible, and there are fewer deep grooves compared to the untreated sample. The wear mechanism appears to be a combination of mild abrasion with some adhesive interactions, as evidenced by the finer debris particles. Upon treatment-optimized parameters in the sample #S5, the wear scar is further reduced compared to both the untreated and #S1 samples, suggesting that under this condition UNSM treatment has further enhanced wear resistance (see Fig. 14 (c1)). As shown in Fig. 14 (c2), the magnified view revealed a relatively smooth wear track with fewer grooves and wear particles, which suggests that the deeper deformed layer through the optimized UNSM treatment effectively resisted the abrasive forces from the W sample. The highest magnification shown in Fig. 14 (c3) presents minimal debris and very fine wear particles indicating that the UNSM treatment in the sample #S5 has led to primarily mild abrasive wear with very limited adhesive interaction. The wear track appears quite smooth, suggesting that the surface has retained much of its integrity and has resisted significant deformation. In summary, as the depth of the deformed layer increases, the wear mechanisms shift from severe abrasive and adhesive wear to primarily mild abrasive wear, with a substantial reduction in wear severity. This progression highlights the effectiveness of UNSM treatments, particularly with optimized conditions, in enhancing the surface hardness and wear resistance of pure W when sliding against a stainless steel 440.

Fig. 15 shows the SEM-EDS images of the wear scar generated on the surface of the counterface ball that came into contact with the untreated and UNSM-treated samples under dry conditions. In the untreated sample Fig. 15 (a1), the wear scar appeared more pronounced with clearer material deformation. In contrast, the UNSM-treated samples shown in Fig. 15 (b1 and c1) exhibited finer, more dispersed wear patterns. The BSE images shown in Fig. 15 (a1, b1 and c1) confirmed that the wear scar size decreased from 730 μm, 690 μm and 610 μm for the untreated, #S1, and #S5 samples, respectively. This reduction means that less wear occurred after UNSM treatment, which further increased the wear resistance by applying UNSM treatment with optimized parameters. The distribution of Fe on the wear scar is shown in Fig. 15 (a2, b2 and c2), which confirms that Fe is sparsely within the wear scar with decreasing intensity for the counterface ball that came into contact with the UNSM-treated samples. This trend suggests less transfer or removal of Fe from the counterface ball in the UNSM-treated samples. The removed Fe from the counterface ball was lesser for the #S5 sample than the #S1 sample. In addition, the untreated sample showed more Fe scattered within the wear scar indicating possible abrasive wear. In contrast, the reduced Fe presence in Fig. 15 (b2 and c2) implies less adhesion due to the modified surface by UNSM treatment. Fig. 15 (a3, b3 and c3) shows the distribution of W on the wear scar, which was transferred from the W sample. It suggests adhesive wear, where material from the W sample adheres to the stainless steel counterface ball. The amount of W transferred appears to decrease in the UNSM-treated samples (see Fig. 15 (b3 and c3)), indicating that the UNSM treatments helped to reduce adhesive wear. The distribution of O on the wear scar is shown in Fig. 15 (a4, b4 and c4). The minimal oxidative wear was confirmed, which does not seem to play a major role at the contact interface. UNSM treatment appears to reduce the wear scar size, limit Fe and W transfer, and result in a more dispersed wear pattern. This implies a shift towards milder abrasive wear with reduced adhesion. The modified surface with a work-hardened surface layer generated by UNSM treatment likely minimizes contact area, decreasing direct metal contact and reducing material transfer.

4. Conclusions

The influence of the UNSM treatment with various parameters on microstructure evolution and tribological properties of the commercially pure W were explored and the primary conclusions are summarized as follows:

- Increasing the static load of the UNSM treatment resulted in a higher density of dislocations and LAGBs fraction, while there was an intermediate optimum value of the vibration amplitude in which materials exhibited more pronounced and homogeneous deformation with maximum depth of deformed layer.
- By repeating the UNSM treatment scan in a perpendicular direction, de-lamination and material removal occurred on the top surface because of the brittle nature and limited work hardening capacity of the material. However, there was a refined region with nanoscale grain size observed beneath the de-laminated area.
- The UNSM treatment led to an increase in the surface hardness and XRD peak broadening. The surface residual stress was also changed from the tensile state of ~ 430 MPa for the untreated sample to a compressive state of ~ −100 MPa after UNSM treatment.
- A significant grain refinement was observed from 4.54 μm for the untreated condition to values less than 0.7 μm for the ultrasonically treated samples. Considering the variation trends of the crystallographic texture, grain boundaries fraction, dislocation density, and average grain size, a grain refinement mechanism including the dislocation polygonization, dynamic recovery, and dynamic recrystallization were suggested.
- The steady-state COF of the untreated sample was 0.62, which was reduced to about 0.50 and 0.42 after UNSM treatment with reference and optimized parameters, respectively. The UNSM treatment with reference and optimized parameters increased the wear resistance of the untreated sample by about 29 % and 38 %, respectively.
- The main wear mechanisms at room temperature were abrasive, adhesive, and fatigue due to the brittleness of W, where the UNSM treatment seemed to have reduced the overall wear severity compared to the untreated sample.

Statement of Originality

The author confirms that the paper entitled *"Effect of Ultrasonic Nanocrystal Surface Modification on Microstructural Evolution and Tribological Properties of Pure Tungsten"* is original, has not been published previously; is not under consideration elsewhere; has the full consent of all authors; and that, if accepted, will not be published elsewhere in the same form, in English or in any other language, without the written consent of the Publisher.

CRediT authorship contribution statement

M. Zohrevand: Data curation, Formal analysis, Methodology, Investigation, Writing – original draft. **J. Likonen:** Conceptualization, Writing – review & editing. **J.W. Coenen:** Conceptualization, Writing – review & editing. **A. Amanov:** Conceptualization, Data curation, Formal analysis, Methodology, Investigation, Writing – original draft, Writing – review & editing, Supervision, Funding acquisition.

Declaration of Competing Interest

The authors declare that they have no known competing financial interests or personal relationships that could have appeared to influence the work reported in this paper.

Acknowledgment

This work made use of Tampere Microscopy Center facilities at

Tampere University. Funding information is not available.

Data availability

Data will be made available on request.

References

[1] Kumar S, Wu CS, Padhy GK, Ding W. Application of ultrasonic vibrations in welding and metal processing: a status review. J Manuf Process 2017;26:295–322.
[2] Zhao Y, Song D, Lin B, Zhang C, Zheng D, Inguva S, Li T, Sun Z, Wang Z, Zhang W. 3D characterization of ultrasonic melt processing on the microstructural refinement of AlCu alloys using synchrotron X-ray tomography. Mater Charact 2019;153:354–65.
[3] Barbosa J, Puga H. Ultrasonic melt processing in the low-pressure investment casting of Al alloys. J Mater Process Technol 2017;244:150–6.
[4] Ashida Y, Aoyama H. Press forming using ultrasonic vibration. J Mater Process Technol 187 2007:118–22.
[5] Yang C, Shan X, Xie T. Titanium wire drawing with longitudinal-torsional composite ultrasonic vibration". Int J Adv Manuf Technol 2016;83(1-4):645–55.
[6] Fereidooni B, Morovvati MR, Sadough-Vanini SA. Influence of severe plastic deformation on fatigue life applied by ultrasonic peening in welded pipe 316 Stainless Steel joints in corrosive environment. Ultrasonics 2018;88:137–47.
[7] Haddadi F, Tsivoulas D. Grain structure, texture and mechanical property evolution of automotive aluminium sheet during high power ultrasonic welding. Mater Charact 2016;118:340–51.
[8] Verma GC, Pandey PM, Dixit US. Modeling of static machining force in axial ultrasonic vibration assisted milling considering acoustic softening. Int J Mech Sci 2018;136:1–16.
[9] Wei L, Wang D. Comparative study on drilling effect between conventional drilling and ultrasonic-assisted drilling of Ti-6Al-4V/Al2024-T351 laminated material. Int J Adv Manuf Technol 2019;103(1-4):141–52.
[10] Zohrevand M, Aghaie-Khafri M, Forouzan F, Vuorinen E. An investigation on microstructure and mechanical properties of 316 stainless steel: a comparison between ultrasonic treatment and thermal annealing. Philos Mag 2022;102(14): 1321–43.
[11] Zohrevand M, Aghaie-Khafri M, Forouzan F, Vuorinen E. Microstructural evolutions under ultrasonic treatment in 304 and 316 austenitic stainless steels: impact of stacking fault energy. Steel Res Int 2021;92(9):2100041.
[12] Samigullina AA, Mukhametgalina AA, Sergeyev SN, Zhilyaev AP, Nazarov AA, Zagidullina YR, Parkhimovich NY, Rubanik VV, Tsarenko YV. Microstructure changes in ultrafine-grained nickel processed by high pressure torsion under ultrasonic treatment. Ultrasonics 2018;82:313–21.
[13] Hu J, Shimizu T, Yoshino T, Shiratori T, Yang M. Evolution of acoustic softening effect on ultrasonic-assisted micro/meso-compression behavior and microstructure. Ultrasonics 2020:106107.
[14] Kumar VC, Hutchings IM. Reduction of the sliding friction of metals by the application of longitudinal or transverse ultrasonic vibration. Tribology Int 2004; 37(10):833–40.
[15] Gu BP, Jin ZD, Kong DJ, Lai JT, Yang ZS, Pan L. Reduction of pulsed-laser surface irradiation induced residual stress using ultrasonic vibration method. Int J Adv Manuf Technol 2017;88:755–65.
[16] Balasubramani N, Venezuela J, Yang N, Wang G, StJohn D, Dargusch M. An overview and critical assessment of the mechanisms of microstructural refinement during ultrasonic solidification of metals. Ultrason Sonochem 2022;89:106151.
[17] Kishore A, John M, Ralls AM, Jose SA, Kuruveri UB, Menezes PrL. Ultrasonic nanocrystal surface modification: processes, characterization, properties, and applications. Nanomaterials 2022;12(9):1415.
[18] Amanov A. Microstructural evolution and mechanical properties of Cu-based alloy by post-sintering ultrasonic nanocrystal surface modification. Mater Lett 2022;308: 131124.
[19] Lee HH, Park HK, Jung J, Amanov A, Kim HS. Multi-layered gradient structure manufactured by single-roll angular-rolling and ultrasonic nanocrystalline surface modification. Scr Mater 2020;186:52–6.
[20] Ye C, Telang A, Gill A, Wen X, Mannava SR, Qian D, Vasudevan VK. Effects of ultrasonic nanocrystal surface modification on the residual stress, microstructure, and corrosion resistance of 304 stainless steel welds. Metall Mater Trans A 2018; 49:972–8.
[21] Li C, Amanov A, Li Y, Wang C, Wang D, Abdel Wahab M. Prediction of residual stress distribution induced by ultrasonic nanocrystalline surface modification using machine learning. Adv Eng Softw 2024;188:103570.
[22] Amanov A. Advancement of tribological properties of Ti–6Al–4V alloy fabricated by selective laser melting. Tribology Int 2021;155:106806.
[23] Karimbaev R, Pyun YS, Amanov A. Fatigue life extension of additively manufactured Nickel-base 718 alloy by nanostructured surface. Mater Sci Eng: A 2022;831:142041.
[24] Amanov A, Berkebile SP. Enhancement of sliding wear and scratch resistance of two thermally sprayed Cr-based coatings by ultrasonic nanocrystal surface modification. *Wear* 512 2023:204555.
[25] Huang B, Ye Y, Wang K, Zhang L, Dong Y, Ye C. Corrosion damage repair of 7075-T6 aluminum alloy by ultrasonic nanocrystal surface modification. Surf Coat Technol 2023;474:130085.
[26] Zhang Q, Hu Z, Su W, Zhou H, Liu C, Yang Y, Qi X. Microstructure and surface properties of 17-4PH stainless steel by ultrasonic surface rolling technology. Surf Coat Technol 2017;321:64–73.
[27] Kim RE, Jeong SG, Ha H, Amanov A, Kim HS. Controlling defects of laser-powder bed fusion processed 316L stainless steel via ultrasonic nanocrystalline surface modification. Mater Sci Eng: A 2023;887:145726.
[28] Jo MC, Yoo J, Amanov A, Song T, Kim SH, Sohn SS, Lee S. Ultrasonic nanocrystal surface modification for strength improvement and suppression of hydrogen permeation in multi-layered steel. J Alloy Compd 2021;885:160975.
[29] Tóth Z, Lovas H. Chemistry of materials science phenomena in high-intensity discharge light sources. Pure Appl Chem 2007;79(10):1771–8.
[30] Yu Y, Song J, Bai F, Zheng A, Peng F. Ultra-high purity tungsten and its applications. Int J Refract Met Hard Mater 2015;53:98–103.
[31] Can F, Courtois X, Duprez D. Tungsten-based catalysts for environmental applications. Catalysts 2021;11(6):703.
[32] Linke J, Du J, Loewenhoff T, Pintsuk G, Spilker B, Steudel I, Wirtz M. "Challenges for plasma-facing components in nuclear fusion. Matter Radiat Extrem 2019;4(5).
[33] Nygren RE, Youchison Dennis L, Wirth BD, Snead LL. A new vision of plasma facing components. Fusion Eng Des 2016;109:192–200.
[34] Xu H, He LL, Pei YF, Jiang CZ, Li WQ, Xiao XH. Recent progress of radiation response in nanostructured tungsten for nuclear application. Tungsten 2021;3: 20–37.
[35] Wu ZM, Zhang J, Huang JC, Fan Y, Yu XH, Zhao YB, Zhu JL, Jin CQ, Wang P, Fu EG. Nanocrystalline W-based alloys with ultrahigh hardness and exceptional irradiation tolerance. Nucl Fusion 2019;59(10):106050.
[36] Wei Q, Jiao T, Ramesh KT, Ma E, Kecskes LJ, Magness L, Dowding R, Kazykhanov VU, Valiev RZ. Mechanical behavior and dynamic failure of high-strength ultrafine grained tungsten under uniaxial compression. Acta Mater 2006; 54(1):77–87.
[37] Wei Q, Zhang HT, Schuster BE, Ramesh KT, Valiev RZ, Kecskes LJ, Dowding RJ, Magness L, Cho K. Microstructure and mechanical properties of super-strong nanocrystalline tungsten processed by high-pressure torsion. Acta Mater 2006;54 (15):4079–89.
[38] Efe M, El-Atwani O, Guo Y, Klenosky DR. Microstructure refinement of tungsten by surface deformation for irradiation damage resistance. Scr Mater 2014;70:31–4.
[39] Guo HY, Xia M, Wu ZT, Chan LC, Dai Y, Wang K, Yan QZ, He MC, Ge CC, Lu J. Nanocrystalline-grained tungsten prepared by surface mechanical attrition treatment: microstructure and mechanical properties. J Nucl Mater 2016;480: 281–8.
[40] Guo HY, Xia M, Chan LC, Wang K, Zhang XX, Yan QZ, He MC, Lu J, Ge CC. Nanostructured laminar tungsten alloy with improved ductility by surface mechanical attrition treatment. Sci Rep 2017;7(1):1351.
[41] Wang H, Xie ZM, Yu ML, Zhao BL, Liu R, Fang QF, Wang XP, Liu CS, Wu X. Ultrafine-grained surface layer of tungsten via a simple two-step microstructure modulation. Int J Refract Met Hard Mater 2024;121:106675.
[42] Zafar I, Merah N, Nouari S, Shuaib AR, N.r Al-Aqeeli. Investigation of wear characteristics of spark plasma sintered W-25wt% Re alloy and W-25wt% Re-3.2 wt% HfC composite. Tribology Int 2017;116:129–37.
[43] Jiang Y, Huang P, Jiang ZQ, Hou J, Xu Z, Wu EH, Li J. Gradient nanostructured tungsten and the thermal shock response. Tungsten 2023;5(4):548–57.
[44] Seyyedi A, Abdoos H. An examination of microstructure and dry wear properties of Nano-Y_2O_3 incorporated in fine-grained W-Ni-Cu alloy prepared by conventional and spark plasma sintering. Int J Refract Met Hard Mater 2022;102:105728.
[45] Jiang Y, Xie ZM, Yang JF, Fang QF. High-temperature tribological behavior of tungsten. Int J Refract Met Hard Mater 2019;84:104992.
[46] Ding CS, Xie XF, Xie ZM, Liu R, Wu XB, Fang QF, Liu CS, Wang XP. Temperature dependence of the friction and wear behavior of pure tungsten. Int J Refract Met Hard Mater 2024:106787.
[47] Banerjee S, Spear J, Dalton PJ. Laser shock peening of tungsten and its dependency on polarisation of light for induced compressive stresses. Opt Express 2022;30(18): 32084–96.
[48] Li W, Shi X, Liang Y, Zhang Z, Cui J. Effects of ultrasonic surface rolling processing on the surface microstructure and properties of a tungsten heavy alloy. Mater Res Express 2019;6(12):1265a5.
[49] Information on: ⟨https://www.plansee.com/en/plansee-group.html⟩.
[50] Wirtz M, Linke J, Loewenhoff Th, Pintsuk G, Uydenhouwen I. Thermal shock tests to qualify different tungsten grades as plasma facing material. Phys Scr 2016;T167: 014015.
[51] Chae JM, Lee KO, Amanov A. Gradient nanostructured tantalum by thermal-mechanical ultrasonic impact energy. Materials 2018;11(3):452.
[52] Zohrevand M, Aghaie-Khafri M, Forouzan F, Vuorinen E. Softening mechanisms in ultrasonic treatment of deformed austenitic stainless steel. Ultrasonics 2021;116: 106519.
[53] Meng D, Zhao X, Li J, Zhao S, Han Q. Mechanical behavior and microstructure of low-carbon steel undergoing low-frequency vibration-assisted tensile deformation. J Mater Res 2017;32(20):3885–93.
[54] Dutta RK, Petrov RH, Delhez R, Hermans MJM, Richardson IM, Böttger AJ. The effect of tensile deformation by in situ ultrasonic treatment on the microstructure of low-carbon steel. Acta Mater 2013;61(5):1592–602.
[55] Nazarov AA, Samigullina AA, Mulyukov RR, Tsarenko YV, Rubanik VV. Changes in the microstructure and mechanical properties of nanomaterials under an ultrasonic wave effect. J Mach Manuf Reliab 2014;43:153–9.
[56] Samigullina A, Nazarov AA, Mulyukov RR, Tsarenko YV, Rubanik VV. Effect of ultrasonic treatment on the strength and ductility of bulk nanostructured nickel processed by equal-channel angular pressing. Rev Adv Mater Sci 2014;39(1).

[57] Bachurin DV, Murzaev RT, Nazarov AA. Relaxation of dislocation structures under ultrasonic influence. Int J Solids Struct 2019;156:1–13.
[58] Zohrevand M, Aghaie-Khafri M, Forouzan F, Vuorinen E. Internal stress relief and microstructural evolution by ultrasonic treatment of austeno-ferritic 2205 duplex stainless steel. Mater Sci Eng: A 2021;815:141290.
[59] Wang F, Guo W, Liu J, Li S, Zhou J. Microstructural evolution and grain refinement mechanism of pure tungsten under explosive loading condition. Int J Refract Met Hard Mater 2014;45:64–70.
[60] Deng HW, Xie ZM, Wang YK, Liu R, Zhang T, Hao T, Wang XP, Fang QF, Liu CS. Mechanical properties and thermal stability of pure W and W-0.5 wt% ZrC alloy manufactured with the same technology. Mater Sci Eng: A 2018;715:117–25.
[61] Kattoura M, Telang A, Mannava SR, Qian D, Vasudevan VK. Effect of ultrasonic nanocrystal surface modification on residual stress, microstructure and fatigue behavior of ATI 718Plus alloy. Mater Sci Eng: A 2018;711:364–77.
[62] Maleki E, Unal O, Guagliano M, Bagherifard Sara. The effects of shot peening, laser shock peening and ultrasonic nanocrystal surface modification on the fatigue strength of Inconel 718. Mater Sci Eng: A 2021;810:141029.